JGR Atmospheres

RESEARCH ARTICLE
10.1029/2023JD039249

Key Points:

- Tube and knot (T&K) dynamics yield faster, more aggressive instability evolutions than axially uniform Kelvin Helmholtz Instabilities (KHI) in stratified shear environments
- T&K-induced twist waves drive the turbulent transition and preclude secondary convective instabilities/KHI that dominate prior laboratory and simulation studies
- T&K-induced turbulence yields faster/larger kinetic energy depletion and entropy production, producing more mixing with weaker efficiency

Supporting Information:

Supporting Information may be found in the online version of this article.

Correspondence to:

T. S. Mixa,
tyler@gats-inc.com

Citation:

Mixa, T. S., Lund, T. S., & Fritts, D. C. (2023). Modeling Kelvin Helmholtz instability tube and knot dynamics and their impact on mixing in the lower thermosphere. *Journal of Geophysical Research: Atmospheres*, *128*, e2023JD039249. https://doi.org/10.1029/2023JD039249

Received 17 MAY 2023
Accepted 14 AUG 2023

Modeling Kelvin Helmholtz Instability Tube and Knot Dynamics and Their Impact on Mixing in the Lower Thermosphere

Tyler S. Mixa[1,2], Thomas S. Lund[2], and David C. Fritts[1,2]

[1]Center for Space and Atmospheric Research (CSAR), Embry-Riddle Aeronautical University, Daytona Beach, FL, USA, [2]Global Atmospheric Technologies and Sciences (GATS)-Inc. Boulder, Boulder, CO, USA

Abstract We present modeling results of tube and knot (T&K) dynamics accompanying thermospheric Kelvin Helmholtz Instabilities (KHI) in an event captured by the 2018 Super Soaker campaign (R. L. Mesquita et al., 2020, https://doi.org/10.1029/2020JA027972). Chemical tracers released by a rocketsonde on 26 January 2018 showed coherent KHI in the lower thermosphere that rapidly deteriorated within 45–90 s. Using wind and temperature data from the event, we conducted high resolution direct numerical simulations (DNS) employing both wide and narrow spanwise domains to facilitate (wide domain case) and prohibit (narrow domain case) the axial deformation of KH billows that allows tubes and knots to form. KHI T&K dynamics are shown to produce accelerated instability evolution consistent with the observations, achieving peak dissipation rates nearly two times larger and 1.8 buoyancy periods faster than axially uniform KHI generated by the same initial conditions. Rapidly evolving twist waves are revealed to drive the transition to turbulence; their evolution precludes the formation of secondary convective instabilities and secondary KHI seen to dominate the turbulence evolution in artificially constrained laboratory and simulation environments. T&K dynamics extract more kinetic energy from the background environment and yield greater irreversible energy exchange and entropy production, yet they do so with weaker mixing efficiency due to greater energy dissipation. The results suggest that enhanced mixing from thermospheric KHI T&K events could account for the discrepancy between modeled and observed mixing in the lower thermosphere (Garcia et al., 2014, https://doi.org/10.1002/2013JD021208; Liu, 2021, https://doi.org/10.1029/2020GL091474) and merits further study.

Plain Language Summary Atmospheric turbulence is challenging to observe and model, but its understanding is pivotal to developing better long-term climate prediction capabilities into general circulation models (GCMs). Turbulence occurs when coherent structures break down into smaller structures that mix with the surrounding air. This mixing behavior determines how energy and momentum are distributed when the large structure breaks down. Because mixing occurs at small scales, GCMs use parameterizations to estimate unresolved mixing without using more resources. This study simulates a representative turbulence event in the thermosphere to learn how to improve mixing parameterizations in GCMs. Regions of strong wind shear generate characteristic turbulence structures called Kelvin Helmholtz Instabilities (KHI). KHI break down through a known sequence of events if they form in artificially-constrained laboratory/simulation environments with uniform wind. Recent studies show that when KHI form in an unconstrained environment like the atmosphere, they develop additional connecting structures known as tubes and knots (T&K). We show that the presence of T&K produces faster turbulence and greater mixing in the thermosphere compared with KHI that form without T&K features. These findings could explain why GCMs underestimate mixing in the thermosphere and will aid the development of more representative turbulence parameterizations in GCMs.

1. Introduction

On 26 January 2018, Kelvin-Helmholtz Instabilities (KHI) were observed at the unusually high altitude of 102 km by a Rocketsonde chemical tracer release over Poker Flat, Alaska (R. L. Mesquita et al., 2020). The KH billows had horizontal wavelengths of λ_h = 9.6 km and rapidly deteriorated from their initial coherent state in a scant 45–90 s, indicating an aggressive underlying shear layer with an approximate half depth of $d \approx \lambda_h/4\pi \approx 800$ m. In situ Rocketsonde wind profiles revealed an apparent superposition of an inertial gravity wave (GW)-induced shear layer and a smaller-scale shear sheet causing the elevated local shear. Lidar measurements from the Poker

Flat Research Range showed a similarly sharp temperature enhancement near the same altitude, yielding a local minimum Richardson number (Ri, see Equation 8) of 0.05 consistent with rapid shear turbulence evolution.

Highly localized multi-scale environments comprised of such "sheet and layer" superpositions are found throughout the atmosphere and have been shown to produce instability events yielding widespread turbulence with elevated dissipation (see e.g., Fritts et al., 2017, and citations therein), yet their contributions to larger-scale mixing and chemical constituent distributions remain largely unknown. General circulation models (GCMs) represent mixing with the vertical eddy diffusion coefficient, K_{zz}, which approximates heat fluxes and transport due to gravity wave breaking but does not address mixing contributions from other sources. K_{zz} is estimated by applying linear saturation theory to a GCM's parameterized gravity wave spectra (Garcia et al., 2007; Liu, 2000); it accounts for turbulence localization with inverse Prandtl number (1/Pr) scaling (e.g., Fritts & Dunkerton, 1985; McIntyre, 1989) but otherwise neglects nonlinear dynamics and subgrid-scale turbulence. The resulting mixing estimates yield a near-50% deficit from observations: WACCM profiles of gravity wave-parameterized K_{zz} show values of 5–50 $m^2\ s^{-1}$ from 80 to 100 km (Liu, 2021) whereas global mean O density profiles measured by the Scanning Imaging Absorption Spectrometer for Atmospheric Chartography (SCIAMACHY) instrument suggest $K_{zz} \sim$ 10–80 $m^2\ s^{-1}$ over 80–100 km (Swenson et al., 2018), a factor of 1.6-2x larger.

Weaker mixing in WACCM mischaracterizes the transport and global distributions of CO_2 and other constituents. CO_2 mixing ratios are consistently too small above 100 km and do not match the observed falloff with altitude (Garcia et al., 2014). Similarly, Na and Fe transport are both under-estimated in WACCM; fluxes of Na and Fe need to be larger to agree with cosmic dust and ablation models (Gardner, 2018). Several efforts have been made to yield greater mixing in GCMs by incorporating parameterized heat fluxes from propagating gravity waves (Gardner, 2018) and reducing Pr to produce better agreement with observations (Garcia et al., 2014). However, Liu (2021) maintains that subgrid-scale dynamics in the MLT account for the majority of the modeled mixing deficit.

Localized shear turbulence events must be considered as a possible mixing source in the mesosphere and lower thermosphere (MLT) to address this mixing deficiency in GCMs. Sharp wind and temperature gradients such as those underlying the Mesquita event exist throughout the atmosphere at scales below the resolution limit of GCMs, and the resulting Ri-critical shear layers produce local instabilities everywhere they occur. Such events arise in multi-scale environments exhibiting what are described as "sheet and layer" structures, which occur throughout the atmosphere into the MLT and which modeling reveals to be prolific sources of local KHI (Fritts & Wang, 2013; Fritts et al., 2013), see for example, Kantha et al. (2017), Doddi et al. (2021), Barat (1982), Sato and Woodman (1982), Lehmacher et al. (2011), and R. L. Mesquita et al. (2020). Though ubiquitous, GCM resolution cannot capture these dynamics (Fritts, Lund, et al., 2022), and their mixing contributions remain unaddressed.

Recent simulations and observations further suggest that many shear-induced instability events undergo "tube and knot" (T&K) dynamics and could account for more mixing than previously attributed to these events. The conventional understanding of KHI evolution assumes billows that are axially uniform, with expected morphologies of turbulence scale progression driven by secondary convective instabilities (CI) forming in the billow cores and secondary KHI in the billow braids (see e.g., Fritts et al., 2014; Klaassen & Peltier, 1985; Peltier & Caulfield, 2003). Real shear layers, however, are not infinitely uniform; variable intensities and depths over their spatial extent will impact the axial coherence of KHI. Laboratory experiments by Thorpe (1987, 2002) showed that even in an artificially uniform environment, KHI "tubes" and "knots" arise and intensify between adjacent, misaligned KH billows prior to the evolution of secondary CI and KHI (see e.g., Fritts et al., 2021a). Over 30 years later, observations by Hecht et al. (2021) revealed KHI T&K dynamics occurring in the MLT, and subsequent modeling and a review of other MLT observational evidence revealed these dynamics to be widespread, perhaps even ubiquitous, in the MLT (Fritts et al., 2021a; Fritts, Wang, Lund, & Thorpe, 2022). However, T&K simulations to-date have only occurred in idealized environments that don't directly correspond to observed atmospheric conditions. Given the potential of KHI T&K dynamics to promote elevated mixing in the MLT, it is imperative to investigate the impact of T&K dynamics on observed shear turbulence events to determine if they can account for the missing mixing modeled in the MLT.

In this study, we evaluate the impact KHI T&K dynamics on the 26 January 2018 thermospheric KHI event reported by R. L. Mesquita et al. (2020). In approximating the observed KHI dynamics we demonstrate how T&K formation accelerates and intensifies billow turbulence evolution to promote enhanced dissipation and mixing. To isolate T&K influences, identically initialized direct numerical simulations (DNS) of the Mesquita

event are conducted with two spanwise (axial) domain sizes: an 8 KHI λ_h domain allowing T&K formation and a 0.5 KHI λ_h domain prohibiting axial non-uniformity. T&K formation is shown to yield rapid proliferation of small-scale turbulent features in places where KH billows link that both form and dissipate at earlier times than the secondary CI/KHI-driven turbulence transition of axially uniform KHI. T&K driven dynamics achieve peak dissipation at twice the speed and amplitude of the equivalent case limited to axially uniform KHI, with similarly enhanced and accelerated mixing. The significant impact of T&K dynamics in this environment suggests extensive contributions to momentum transport and deposition that could aid the development of improved mixing parameterizations in GCMs.

The remainder of the paper is organized as follows: Section 2 presents a description of the numerical methods, including the governing equations, solution method, and simulation parameters employed by our numerical model; the procedure to determine representative initial conditions from the available observations; and the nondimensional parameters defining the simulation environment. Simulation results are presented in Section 3, evaluating the instability characteristics, dissipation and energy exchange, and mixing characteristics promoted by T&K dynamics relative to their absence. Section 4 contains the summary and conclusions of our results.

2. Numerical Methods

2.1. CGCAM Model Architecture

Simulations herein are conducted using the Complex Geometry Compressible Atmosphere Model (CGCAM). CGCAM solves the nonlinear, compressible Navier-Stokes equations, written in divergence form as:

$$\frac{\partial \rho}{\partial t} + \frac{\partial (\rho u_j)}{\partial x_j} = 0 \tag{1}$$

$$\frac{\partial (\rho u_i)}{\partial t} + \frac{\partial (\rho u_i u_j)}{\partial x_j} = -\frac{\partial p}{\partial x_i} - \rho g \delta_{i3} + \frac{\partial \sigma_{ij}}{\partial x_j} \tag{2}$$

$$\frac{\partial \rho E}{\partial t} + \frac{\partial \left[(\rho E + p) u_j\right]}{\partial x_j} = -\rho g u_3 + \frac{\partial (u_i \sigma_{ij})}{\partial x_j} - \frac{\partial q_j}{\partial x_j} \tag{3}$$

where σ_{ij} and q_j are the viscous stress and thermal conduction, defined as

$$\sigma_{ij} = \mu \left[\left(\frac{\partial u_i}{\partial x_j} + \frac{\partial u_j}{\partial x_i} \right) - \frac{2}{3} \left(\frac{\partial u_k}{\partial x_k} \right) \delta_{ij} \right] \quad \text{and} \quad q_j = -\kappa \frac{\partial T}{\partial x_j}. \tag{4}$$

Here μ is the dynamic viscosity, κ is the thermal conductivity, and δ_{ij} is the Kronecker delta. μ and κ depend on the temperature through Sutherland's Law (White, 1974). The solution variables are the air density ρ, the momentum per unit volume ρu_i or $(\rho u, \rho v, \rho w)$ with velocity components $(u_i, u_j, u_k) = (u, v, w)$ along (x, y, z). Energetics and entropy are discussed in Section 3.3.

We assess the evolution of instability features via the vorticity magnitude

$$|\zeta| = |\nabla \times u| \tag{5}$$

and the intermediate eigenvalue λ_2 of the tensor

$$\mathcal{H} = \mathcal{S}^2 + \mathcal{R}^2 \tag{6}$$

(see e.g., Jeong & Hussain, 1995), where $\mathcal{S}$ and $\mathcal{R}$ are the strain and rotation rate tensors, with components defined as

$$\mathcal{S}_{ij} = \frac{1}{2} \left(\frac{\partial u_i}{\partial x_j} + \frac{\partial u_j}{\partial x_i} \right) \quad \text{and} \quad \mathcal{R}_{ij} = \frac{1}{2} \left(\frac{\partial u_i}{\partial x_j} - \frac{\partial u_j}{\partial x_i} \right). \tag{7}$$

$|\zeta|$ and $|\lambda_2 < 0|$ reveal the dominant features with strong rotational tendencies, enabling the visualization of emerging KHI, T&K, and twist waves as the flow becomes turbulent.

Solution variables are stored at the cell centroids, and fluxes on the faces are constructed using a kinetic energy-conserving interpolation scheme similar to that discussed in Felten and Lund (2006) for the incompressible Navier-Stokes equations. The governing equations are discretized using the finite-volume framework, in which

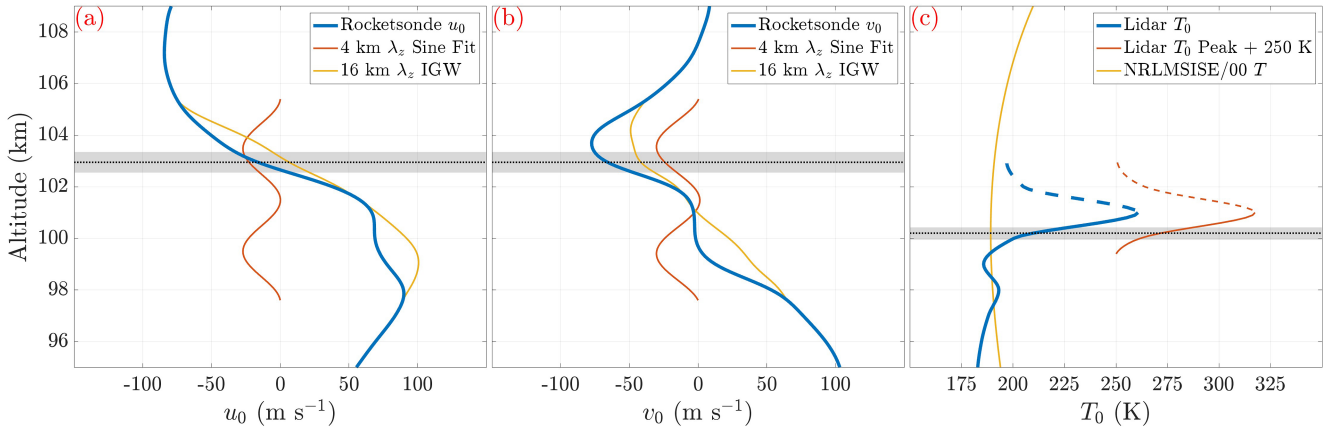

Figure 1. Rocketsonde and lidar profiles (blue curves) and decompositions (orange and yellow curves) from the R. L. Mesquita et al. (2020) KHI event. Rocketsonde profiles have been smoothed with a 20 point Gaussian window. Shaded regions indicate layers of peak shear and stability underlying the profiles.

each computational cell is considered to be a small control volume. The resulting scheme is globally conservative for mass, momentum, total energy, and kinetic energy. Time advancement is achieved via a low-storage, third-order accurate Runge-Kutta scheme with a variable time-step satisfying the CFL stability condition. Additional details for CGCAM are provided by Dong et al. (2020) and Lund et al. (2020).

The model domains employed in these simulations extend 40 km in the streamwise (x) direction (4 KHI λ_h) and from 90 to 115 km in altitude (z). To enable direct comparisons of cases with and without T&K dynamics, DNS were conducted with two spanwise (y, axial) domain sizes: an 80 km (8 KHI λ_h) domain allowing T&K formation and a 5 km (0.5 KHI λ_h) domain prohibiting axial non-uniformity. The domain employs periodic horizontal boundary conditions and characteristic vertical boundary conditions. 2.5 km sponge layers at the top and bottom of the vertical domain constrain the useable domain to $92.5 < z < 112.5$ km. Each simulation is executed on Department of Defense high-performance supercomputers with a (Nx, Ny$_1$, Ny$_2$, Nz) = (1,824, 3,648, 228, 1,152) grid, having streamwise and spanwise grid resolution of (Δx, Δy) = 21.9298 m and Δz = 21.7014 m. To seed the instability formation, a white noise spectrum is added to the initial background wind field with a root mean square amplitude of 10^{-3} m s^{-1}.

2.2. Defining Representative Initial Conditions

The observational datasets capturing the R. L. Mesquita et al. (2020) KHI event include wind profiles triangulated from the Rocketsonde TMA chemical release, temperature profiles from the nearby Poker Flat Na lidar, and remote imaging of the Rocketsonde chemical tracer release revealing the KHI evolution. Raw profiles from the Rocketsonde and Na lidar (blue curves) and profile decompositions (orange and yellow curves) are shown in Figure 1, and the modified initial conditions for the simulations are shown in Figure 2. Rocketsonde zonal and meridional wind profiles (u_0 and v_0, Figures 1a and 1b) display rotary tendencies indicating an inertial gravity wave (IGW) with a compressed phase structure generating a narrow region of enhanced vertical shear ($\partial U_0/\partial z$) near 103 km, where U is the total horizontal wind. Sinusoidal decomposition of the winds (Figures 1a and 1b) reveals a likely-transient 4 km λ_z sinusoidal enhancement (orange curves) increasing the local shear of the background 16 km λ_z IGW (yellow curves) where their phases align. The superposition yields a shear layer at 102.5 km with 0.00827 s^{-1} amplitude and ~800 m characteristic depth indicated by the gray shaded regions in Figures 1a and 1b. The nearby Na lidar temperature profile (T_0, Figure 1c) shows local maximum at 101 km. The temperature profile is spatially offset from the Rocketsonde measurement but roughly coincident in time. Lidar data indicates significant temporal variability, with peak T shifting ±20 K and ±2 km in the hour surrounding the event. The dashed line at the top of the profile indicates a region where a low signal to noise ratio could compromise the accuracy of the measured lapse rate. However, lapse rates from the NRLMSISE/00 empirical model employed by R. L. Mesquita et al. (2020) conservatively estimate a minimum Richardson number of 0.05 near the KHI altitude. The lapse rate in the reliable region of the data yields a stability (N^2) layer at 100.2 km (gray shading in Figure 1c), where N is the Brunt-Väisälä frequency. The stability layer has a 0.00279 s^{-2} amplitude and a characteristic depth of ~500 m, 2.3 km lower and 300 m shallower than the shear layer in the Rocketsonde winds.

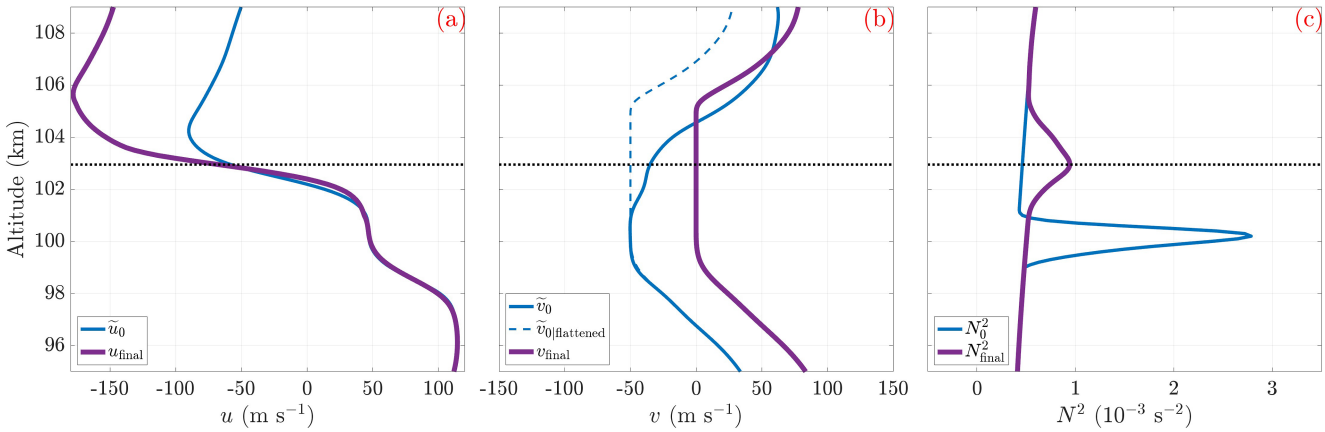

Figure 2. Original and modified background profiles of u, v, and N^2 used to initialize the simulations. Variables are plotted in the rotated coordinate frame of the simulation domain.

KHI revealed by the chemical tracer exhibit $\lambda_h = 9.6$ km and rapidly deteriorate in 45–90 s. We expect the original layer that excited these KHI comprised collocated shear and stability layers with equal characteristic scales of $d \approx \lambda_h/4\pi = 800$ m and amplitudes yielding the underlying Ri. The observed shear and stability layers are offset in altitude and have different depths, suggesting that the transient components of u, v, and T have evolved away from the KHI source layer characteristics at the times and locations of their observation. To simulate the observed KHI, we approximate the prior state of the layers from the existing profiles by modifying the transient components (Figure 1, orange curves) of u, v, and T to match the inferred KHI source characteristics.

The methodology for generating the input profiles is the following: (a) Sinusoidal decomposition of the Rocketsonde winds isolated the transient 4 km λ_z components of u and v. (b) An NRLMSISE/00 empirical temperature profile (Figure 1c, yellow curve) was subtracted from T_0 to isolate the transient temperature peak in the lidar data (Figure 1c, orange curve) corresponding to the sinusoidal local wind enhancements. (c) The lidar temperature peak was then superposed on the model temperature profile at the altitude of peak shear to collocate the layers underlying the KHI. (d) The vertical depth of the underlying stability peak was then increased to 800 m, matching the shear depth and the inferred source layer depth of the observed KHI. (e) The collocated layers have a minimum Ri of 0.41, so the transient wind and temperature gradients at the layer were amplified (reduced) to increase (decrease) the shear-squared (stability) amplitude by $\sim\sqrt{8}$ and yield a minimum Richardson number of Ri = 0.05. (f) To retain the initial background characteristics above the layer, wind/temperature profiles above their modified peaks were extended vertically with the same vertical shear and stability found above the initial layers. (g) For numerical convenience, the final wind components were rotated 45° to have maximum shear in the streamwise (x) direction at the layer, and the spanwise (y) component of the rotated winds having minimum shear was set to 0 m s^{-1} to prevent spanwise feature advection. Figure 2 shows the measured wind and stability profiles in the rotated domain $\left(\widetilde{u}_0, \widetilde{v}_0, N_0^2\right)$ and the resulting modified profiles $\left(u_{\text{final}}, v_{\text{final}}, N_{\text{final}}^2\right)$ used to initialize CGCAM runs, where u and v are the wind components in the x (streamwise) and y (spanwise) coordinate directions of the simulation domain.

2.3. Derived Layer and Nondimensional Parameters

The layer characteristics of the background profiles are shown in Figure 3, including $\left(\frac{\partial U}{\partial z}\right)^2$, N^2, and Ri. Shear and stability profiles for the collocated layers are shown in Figures 3a and 3b, with 800 m scaled sech^2 and sech^4 profiles (dashed lines) confirming the layer half depth of the input profiles. The Richardson number is given by

$$Ri = N^2 / \left(\frac{\partial U}{\partial z}\right)^2 \tag{8}$$

and shown in Figure 3c. The minimum value of $Ri = 0.05$ occurs at the layer center at 102.9 km.

The Reynolds number is calculated from the shear layer half depth d as

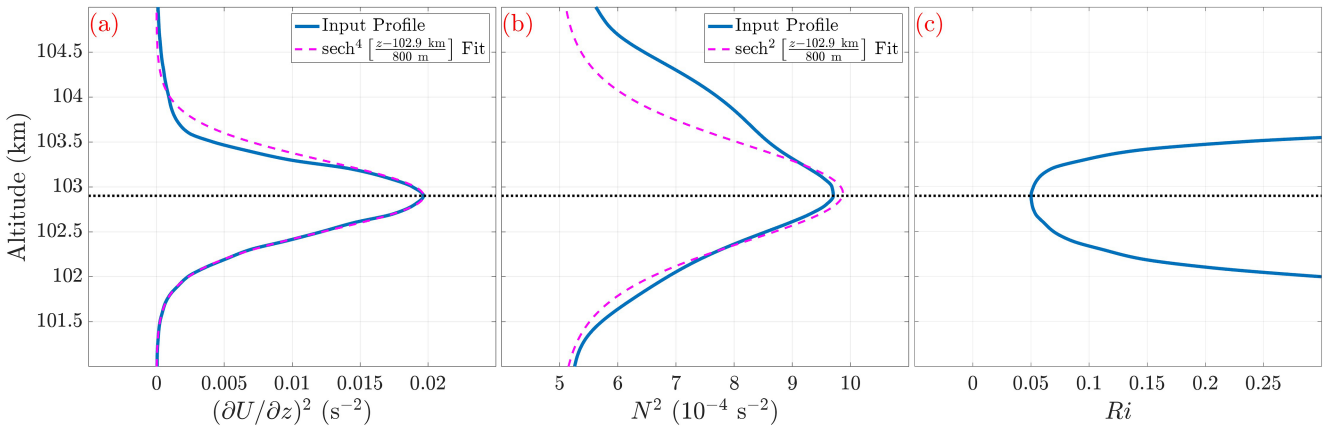

Figure 3. Profiles of the squared vertical shear $\left(\frac{\partial U}{\partial z}\right)^2$, stability N^2, Richardson number Ri, and their associated 800 m fits.

$$\mathrm{Re} = \frac{\rho\, d\Delta U/2}{\mu}, \tag{9}$$

where ΔU is the velocity difference over the shear layer and μ is the kinematic viscosity. μ is calculated via Sutherlands Law (White, 1974) from the ground reference value $\mu_0 = 1.506 \times 10^{-5}$ m^2 s^{-1} and the background temperature and density. Peak values of Re = 2,200 at the layer support the formation of both secondary CI and secondary KHI for this low Ri.

Simulations indicated peak horizontally-averaged kinetic energy dissipation rates per unit mass of $\epsilon_m = 2$–3 W kg^{-1} and a corresponding Kolmogorov length scale of

$$\eta = \left(\nu^3/\epsilon_m\right)^{\frac{1}{4}} \approx 12 \text{ m}. \tag{10}$$

The domain grid spacing of $\Delta\mathbf{x} \approx 22$ m results in a resolution ratio of $R = \Delta\mathbf{x}/\eta = 1.83$ which satisfies the DNS criteria of $R \approx 1.5$–2.1 (Moin & Mahesh, 1998; Pope, 2000). Hence, true DNS is achieved and no subgrid-scale turbulence parameterization is required.

3. Results

The purpose of the numerical results is to demonstrate how T&K features follow distinct instability pathways that evolve faster, dissipate more energy, and yield more mixing than axially uniform KHI. Section 3.1 presents the instability morphologies of the T&K-allowing DNS, showing how misaligned billow junctions and axial non-uniformity lead to T&K feature superpositions that quickly become turbulent and engulf the domain. Section 3.2 identifies the equivalent instability evolutions in a smaller horizontal domain consistent with previous KHI DNS, where the narrower spanwise dimension precludes axial billow deformations that would otherwise enable T&K dynamics. Here the turbulence is dominated by characteristic secondary CI/KHI and billow pairing as seen in previous studies, dynamics that are precluded by the rapid evolution of T&K-induced dissipation in the wider domain DNS. Section 3.3 compares the dominant dissipation, entropy, and energy exchange metrics in both DNS, demonstrating how both instantaneous and integrated metrics mirror the dominant instability features and yield larger values for the T&K case. Section 3.4 introduces and evaluates the mixing efficiency of both events using several standard metrics, showing how T&K dynamics produce more mixing but do so at weaker assessed efficiencies.

3.1. Instability Differentiation With T&K

Horizontal overviews (Figure 4) of the vorticity magnitude $|\zeta|$ and intermediate eigenvalue λ_2 in the T&K-allowing DNS reveal spanwise KH billow deformation sites exciting T&K evolutions and twist waves. The horizontal

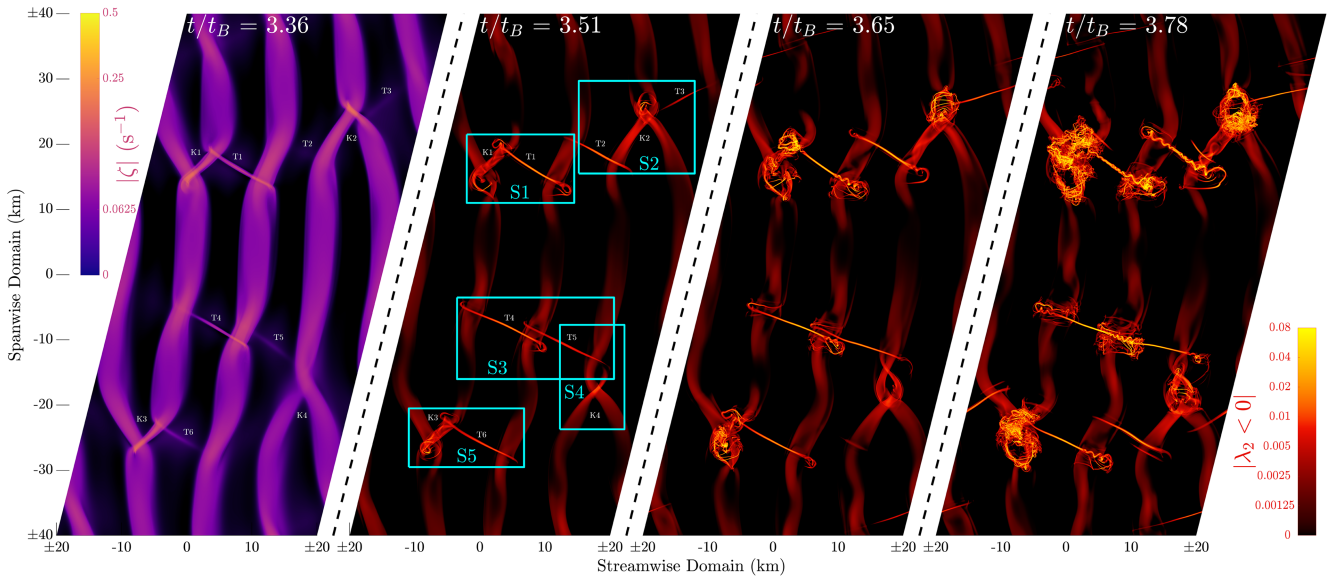

Figure 4. Horizontal cross-sections of the vorticity magnitude (ζ, left) and intermediate eiganvalue of Equation 6 (λ_2, right panels; see Section 2.1) showing T&K evolution from 3.36 to 3.78 t_B. Labeled features are described in the text. See Movies in Supporting Information S1 for additional times.

domain is presented in a parallelogram orientation, shifting the center location of the periodic streamwise domain from $x = 0$ km to $x = \pm 20$ km along the spanwise extent of the domain. This display format retains the full extent of the x-y domain in a single plot while elucidating the relative locations of vorticity features straddling the streamwise boundaries. Along the spanwise axis, initial KH billows in panel 1 exhibit local variations in $|\zeta|$ orientation leading to lateral junctions where adjacent billows are misaligned. These distorted billow regions form characteristic T&K structures consistent with (Fritts, Wang, Lund, & Thorpe, 2022; Fritts, Wang, Thorpe, & Lund, 2022) that locally elevate $|\zeta|$:

1. horizontally rotated KH billows produce "billow linking" vortex tubes connecting pairs of streamwise-adjacent billows at marked locations T1-T6; and
2. regions where 2 billows link to 1 (2:1) produce "billow merging" vortex knots in a loop connecting the three spanwise-adjacent billows at marked locations K1-K4.

Each site identified in panel 2 hosts a unique superposition of T&K features connecting up to 5 adjacent KH billows:

- Sites S1 and S5 have a vortex knot with a vortex tube linking one leg of the knot to the adjacent billow at larger x;
- Site S2 has a vortex knot with a vortex tube linking one leg to the adjacent upstream billow and another vortex tube linking the knot core to the adjacent downstream billow;
- Site S3 has two vortex tubes linking the central billow to both the upstream and downstream billows; and
- Site S4 has a vortex knot with a vortex tube shared with S3 linking the knot core to the adjacent upstream billow.

All five T&K superposition sites break down the parent vortices into mode 1 and mode 2 Kelvin vortex waves referred to here as twist waves (Kelvin, 1880), instability structures comprising radial displacements that rotate along the vortex axis as they propagate away from the initial location. Mode 1 twist waves start with a single radial displacement that distorts a cylindrical vortex filament into a helix as it propagates, and mode 2 twist waves split the vortex filament with a pair of radial displacements that differentially advect each other to form a double helix. Panels 2–4 of Figure 4 exhibit several characteristic twist wave evolutions for similar sets of T&K feature superpositions. Billow linking vortex tubes (T1–T6) produce pairs of mode 1 twist waves that propagate from the linked billows toward the tube centers in panels 3–4. Billow merging vortex knots having one leg linked to an adjacent billow at Sites S1, S2, and S5 form mode 2 twist waves in the linked leg of the knot (intersection K1-T1 at S1 and intersection K3-T6 at S5 in panels 2–4; intersection T2-K2 at S2 in panels 3–4). Larger mode

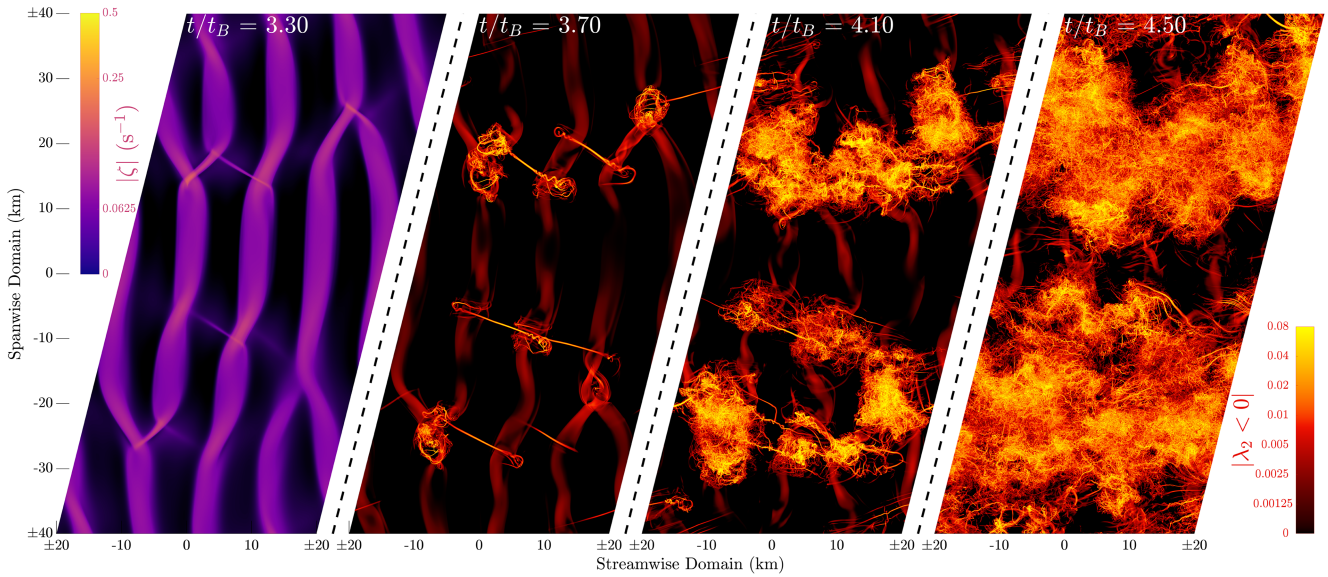

Figure 5. As in Figure 4 for 3.30–4.50 t_B.

2 twist waves also form at Sites S2 and S4 on the single-leg side of 2:1 knots K2 and K4. Knot cores (K1–K4) also exhibit fragmentation as small scale, adjacent vortices become intertwined. All of these processes yield finer scale, higher amplitude vorticity structures that drive the transition to turbulence.

Instability sites produced by T&K dynamics generate local, rapidly expanding turbulence regions that quickly engulf the entire horizontal extent of the shear layer. Figure 5 shows horizontal overviews of the event in the manner of Figure 4, demonstrating the evolution of widespread turbulence from the initial T&K sites (a full video can be found in Supporting Information S1). Initial billow distortions in panel 1 quickly develop T&K features that develop mode 1 and mode 2 twist waves (panel 2). Mode 2 twist waves and the interaction of mode 1 twist waves with adjacent, orthogonal KHI cause fragmentation of KH billow cores. Twist wave-induced fragmentation yields smaller scale, intensified vortical structures, and successive like interactions drive the transition to turbulence as they proliferate in all directions from their source sites (panel 3). Losing their initial anisotropy, regions of intense turbulence merge and entrain most of the shear layer into large, well-mixed regions (panel 4). Turbulence regions promoted by T&K dynamics are notably more aggressive than streamwise swaths of near-axial uniformity at $y = 0$ and $y = \pm 40$ km, suggesting that T&K dynamics yield more vigorous and intensified turbulence than KHI events constrained to be axially uniform. The evolutions and linkages that lead to intensified T&K dynamics appear to preclude the potential for secondary CI seen in the axially uniform KHI at later times.

3.2. Instability Evolution in Axially Uniform KHI

Comparing KHI cross sections from the T&K-allowing DNS with the T&K-prohibiting DNS conclusively shows the radical departures of T&K evolutions from equivalently initialized, axially uniform KHI. Streamwise-vertical slices (Figures 6a–6d) of the temperature perturbations (T') at $y = 20$ km in the T&K-allowing DNS reveal the following crucial deviations from domain center T' slices in the T&K-prohibiting DNS (Figures 6e–6h) at the same times:

1. Though initial KHI in both cases (Figures 6a and 6e) evolve at similar times and scales, KHI in the T&K-allowing cross-sections develop secondary instability structures (Figure 6b) while the T&K-prohibiting KHI remain coherent (Figure 6f).
2. At the latter two times (Figures 6c–6d and 6g–6h), the T&K-allowing case is already well-mixed by the time the T&K-prohibiting case shows signs of weak tertiary instability structures in the periphery of the billow cores.

w' and T' cross-sections of the T&K-prohibiting DNS in Figure 7 reveal billow merging that delays secondary CI/KHI formation and elicits stirring oscillations within the billow cores. Billow merging at 4.76 t_B (Figures 7b

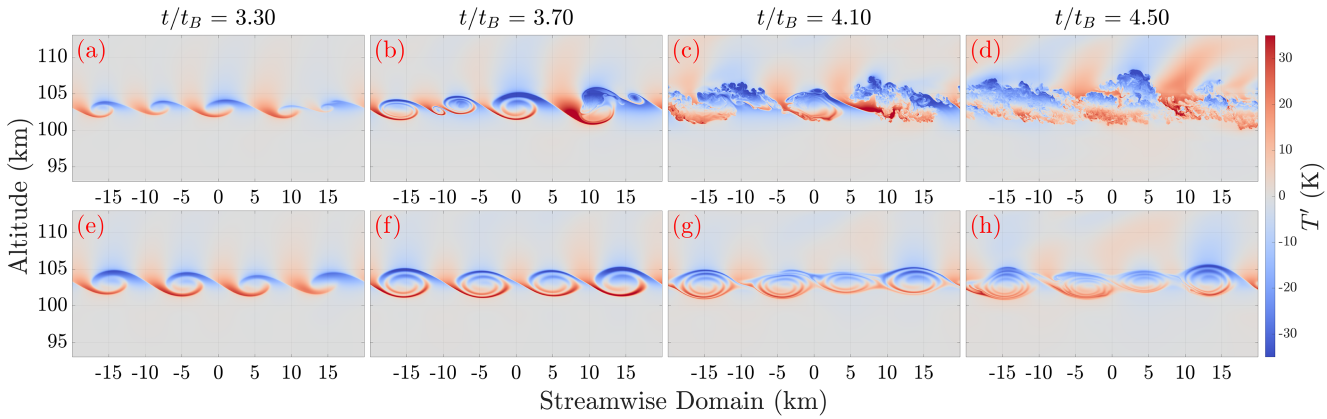

Figure 6. Vertical cross-sections of the temperature perturbation (T') fields comparing KHI evolution in the T&K-allowing (top) and T&K-prohibiting (bottom) DNS results. Times correspond to the four panels in Figure 5.

and 7f) reduces the number of KHI billows in the streamwise domain from 4 to 3. As the two central billows merge, their perturbation amplitudes weaken relative to earlier times (Figures 7a and 7e), further delaying instability onset. Spanwise cross-sections at $z = 103$ km show no indications of secondary CI formation until after 4.76 t_B (Figures 7i–l), long after turbulence has fully engulfed the T&K-allowing domain in Figure 6. Prominent secondary KHI form at the top of the billows at 5.61 t_B (Figures 7d and 7h), driving the transition to turbulence a full 2 t_B after the initial billow formation. Within the billows, peak amplitude regions of T' (w') in the billow core advect horizontally (vertically) about the vertical (horizontal) billow core axis rather than immediately dissipating. These oscillatory motions delay the fully mixed state of horizontal homogeneity to much later times as the entrained fluid stirs about the billow core for several buoyancy periods (a full video can be found in Supporting Information S1).

3.3. Dissipation and Energy Exchange Differentiation With T&K

To evaluate turbulence and mixing characteristics, we compare the dominant terms of entropy creation and energetic exchange in the two DNS cases. The production of volume-averaged entropy, neglecting boundary fluxes, is given by

$$\Delta S = \int \left(\left\langle \frac{\epsilon}{T} \right\rangle + \left\langle \frac{\chi}{T^2} \right\rangle \right) dt, \tag{11}$$

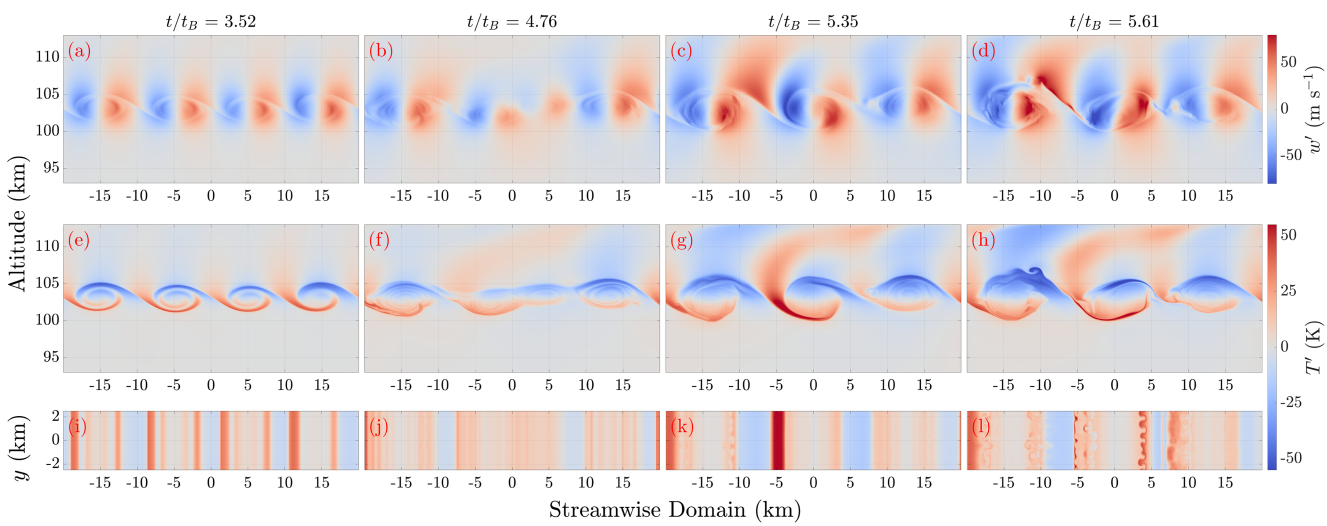

Figure 7. Vertical w' cross-sections (top), vertical T' cross-sections (middle), and horizontal T' cross-sections (bottom) in the T&K-prohibiting DNS results.

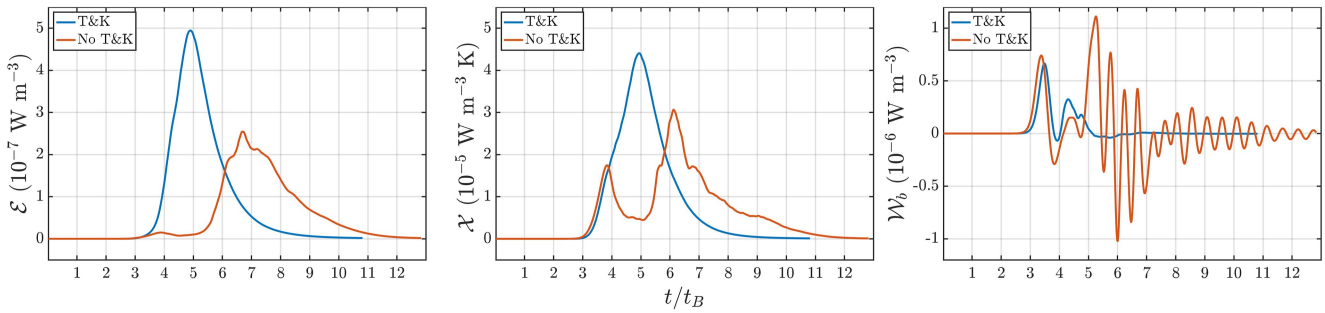

Figure 8. Instantaneous domain-averaged mixing parameters for the T&K-allowing and T&K-prohibiting DNS.

where $\epsilon = \sigma_{ij} S_{ij}$ is the kinetic energy dissipation rate, $\chi = k\left(\frac{\partial T}{\partial x_k}\frac{\partial T}{\partial x_k}\right)$ is the thermal energy dissipation rate, and $\langle\rangle$ indicates volume averaging. $\mathcal{E} = \langle\epsilon\rangle$ is a marker for the onset of 3D turbulence, while $\mathcal{X} = \langle\chi\rangle$ is an approximate metric for perturbation amplitude growth in the dominant instabilities. The volume-averaged total energy is given by

$$E = KE + PE + IE, \tag{12}$$

where $KE = \langle \rho u_k u_k / 2 \rangle$ is the volume-averaged kinetic energy, $PE = \langle \rho g z \rangle$ is the volume-averaged potential energy, $IE = c_v \langle T \rangle$ is the volume-averaged internal energy, and c_v is the specific heat at constant volume. We also assess mixing via energy exchange from kinetic energy to potential and internal energy:

$$\Delta KE_{|KE \Leftrightarrow PE} = \int \mathcal{W}_b \, dt, \tag{13}$$

where $\mathcal{W}_b = \langle \rho g w' \rangle$ is the volume-averaged buoyancy work, and

$$\Delta KE_{|KE \Leftrightarrow IE} = \int (\mathcal{E} - \mathcal{W}_{pv}) dt, \tag{14}$$

where $\mathcal{W}_{pv} = \left\langle p \frac{\partial u_k}{\partial x_k} \right\rangle$ is the volume-averaged pressure-volume work. Here we note that of the energy exchange quantities, only ϵ represents a positive-definite, irreversible ($\rightharpoonup$) depletion of KE; $\mathcal{W}_b$ and $\mathcal{W}_{pv}$ both constitute bidirectional energy exchange ($\Leftrightarrow$), but their final equilibrium states ($\rightleftharpoons$) can be assessed as irreversible work once turbulence subsides.

Figure 8 shows the time evolution of $\mathcal{E}$, $\mathcal{X}$, and $\mathcal{W}_b$ for both DNS. Faster instability evolution in the T&K-allowing case yields more vigorous dissipation: T&K-driven turbulence achieves a peak dissipation rate of $\mathcal{E} = 4.95 \times 10^{-7}$ W m^{-3} at 4.91 t_B, 94% larger and 1.8 t_B earlier than the secondary CI/KHI-driven turbulence in the T&K-prohibiting DNS ($\mathcal{E} = 2.55 \times 10^{-7}$ W m^{-3} at 6.68 t_B). These results expand on the dissipation analysis of Fritts, Wang, Lund, and Thorpe (2022) and Fritts, Wang, Thorpe, and Lund (2022) and definitively disprove the long-held notion that secondary CI are the primary trigger of enhanced dissipation in stratified shear environments (see e.g., Klaassen & Peltier, 1985; Caulfield & Kerswell, 2000; Peltier & Caulfield, 2003, and citations therein). $\mathcal{X}$ evolutions identify rapid instability amplitude growth accompanying the $\mathcal{E}$ peak in the T&K-allowing DNS, but $\mathcal{X}$ in the T&K-prohibiting DNS is markedly different, decreasing after its initial increase at ~3 t_B until the onset of elevated $\mathcal{E}$ at ~6 t_B. The decrease is correlated with the billow merging identified in Figure 7, showing how merging and slower secondary CI/KHI growth delay dissipation to later times in the absence of T&K dynamics. $\mathcal{W}_b$ in the T&K-allowing DNS is predominantly positive, but it is dwarfed by the periodic positive and negative oscillations in the T&K-prohibiting DNS after 5 t_B. These $\mathcal{W}_b$ oscillations correspond to stirring motions identified in Figure 7 (panels c–d; g–h) for the T&K-prohibiting DNS; though the oscillations have higher absolute amplitudes than in the T&K-allowing DNS, a significant portion of $\mathcal{W}_b$ in the T&K-prohibiting DNS is reversible and does not contribute to the net mixing in the final state of the flow.

Accumulated mixing parameters in Figure 9 show markedly higher event-level dissipation, entropy production, and kinetic energy conversion enabled by T&K dynamics. Comparable final states are identified by equivalent $\mathcal{E}$ values, where the T&K-allowing DNS produces 31% larger accumulated $\mathcal{E}$, 12% larger accumulated $\mathcal{X}$, and 23%

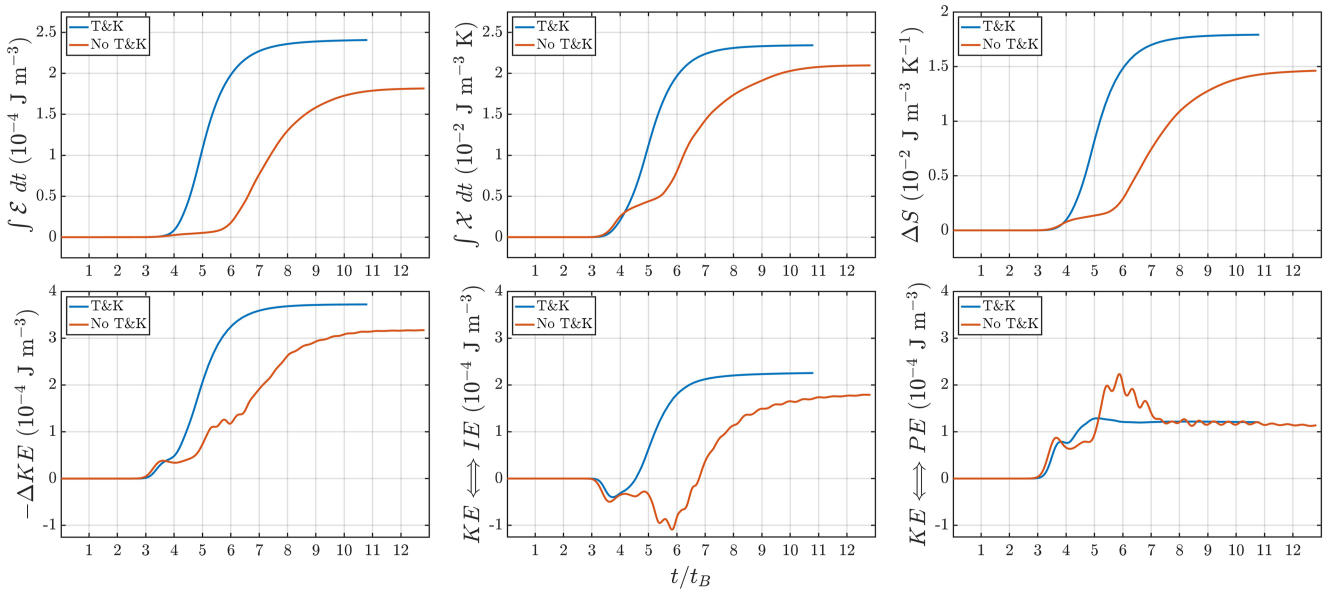

Figure 9. Integrated domain-averaged mixing parameters for the T&K-allowing and T&K-prohibiting DNS, including the resulting ΔS, ΔKE, and the partitioned KE exchanges with IE and PE.

larger ΔS than the T&K-prohibiting DNS. ΔKE is also 17% larger in the T&K-allowing DNS, driven primarily by larger and faster $\mathcal{E}$ growth. The partitioned KE exchanges (last two panels) are both non-monotonic, indicating reversible exchanges via positive $\mathcal{W}_{pv}$ and negative $\mathcal{W}_b$. Time evolution of the $KE \Leftrightarrow IE$ energy exchange shows an initial KE increase in both cases (negative values) due to elevated $\mathcal{W}_{pv}$ during the initial KHI rollup. The duration and amplitude of $IE \Rightarrow KE$ are larger in the T&K-prohibiting DNS due to the longer duration of KHI billow coherence, but both cases eventually produce net $KE \rightharpoonup IE$ after the onset of turbulence. The $KE \Leftrightarrow PE$ exchange confirms that much of the $\mathcal{W}_b$ in the T&K-prohibiting case after 5 t_B is reversible; though it achieves a larger accumulated $KE \Rightarrow PE$ at 6 t_B, the final $KE \rightleftharpoons PE$ state restores the stirred energy back to KE, producing a $KE \rightharpoonup PE$ deficit of 6% relative to the T&K-allowing case. The mixing implications of these results are discussed below.

3.4. Mixing Efficiency Differentiation With T&K

Broadly, the mixing efficiency γ of a turbulence event is assessed as a ratio of the increase in potential energy to the expended kinetic energy in the final equilibrium state, that is,

$$\gamma_E = \frac{\Delta PE}{-\Delta KE} \tag{15}$$

(Gregg et al., 2018). Though K_{zz} is useful as an aggregate atmospheric measure in GCMs, γ is the more suitable tool for assessing DNS and can be estimated with K_{zz} from GCMs or observations via the equilibrium assumption methods of T. R. Osborn and Cox (1972) or those of Weinstock (1978), T. Osborn (1980). Equation 15 is often simplified to

$$\gamma_{\mathcal{W}} = \frac{\int \mathcal{W}_b\ dt}{\int \mathcal{E}\ dt} \tag{16}$$

with the similarly derived flux Richardson number R_f expressed as

$$R_{f|\mathcal{W}} = \frac{\int \mathcal{W}_b\ dt}{\int (\mathcal{W}_b + \mathcal{E}) dt} \tag{17}$$

to be bounded by 1. In Boussinesq flows, Equations 16 and 17 represent the net energy exchanges $KE \rightleftharpoons PE$ and $KE \rightleftharpoons IE$ in the final equilibrium state. The equivalent expressions for a compressible environment are then

Table 1
Event Mixing Efficiency Parameters

Parameter	Unit	T&K prohibited	T&K allowed	% change[a]
ΔPE	J m^{-3}	9.23×10^{-5}	1.02×10^{-4}	+10%
ΔKE	J m^{-3}	-3.17×10^{-4}	-3.72×10^{-4}	+17%
γ_E	–	0.29	0.27	−6%
$\int \mathcal{W}_b\, dt$	J m^{-3}	1.14×10^{-4}	1.21×10^{-4}	+6%
$\int \mathcal{E}\, dt$	J m^{-3}	1.84×10^{-4}	2.40×10^{-4}	+31%
$\gamma_{\mathcal{W}}$	–	0.62	0.50	−19%
$R_{f\|\mathcal{W}}$	–	0.38	0.33	−13%
$\int (\mathcal{E} - \mathcal{W}_{pv})dt$	J m^{-3}	1.79×10^{-4}	2.26×10^{-4}	+26%
γ_{KE}	–	0.64	0.53	−16%
$R_{f\|KE}$	–	0.39	0.35	−10%
$\overline{D}_{APE}$	J m^{-3}	8.87×10^{-5}	8.75×10^{-5}	−1%
$\overline{D}_{KE}$	J m^{-3}	9.99×10^{-5}	1.70×10^{-4}	+70%
γ_{APE}	–	0.89	0.51	−42%
$R_{f\|APE}$	–	0.47	0.34	−28%
$\int \langle \chi / T^2 \rangle dt$	J m^{-3} K^{-1}	5.45×10^{-7}	5.90×10^{-7}	+8%
$\int \langle \epsilon / T \rangle dt$	J m^{-3} K^{-1}	9.17×10^{-7}	1.20×10^{-6}	+31%
γ_S	–	0.59	0.49	−18%
$R_{f\|S}$	–	0.37	0.33	−12%

[a]Calculated with respect to the T&K prohibited value as 100%.

$$\gamma_{KE} = \frac{\int \mathcal{W}_b\, dt}{\int (\mathcal{E} - \mathcal{W}_{pv})dt} \quad \text{and} \quad R_{f|KE} = \frac{\int \mathcal{W}_b\, dt}{\int (\mathcal{W}_b + \mathcal{E} - \mathcal{W}_{pv})dt} \tag{18}$$

utilizing the ΔKE partition in Equations 13 and 14. Winters et al. (1995) proposed the alternate metric of available potential energy

$$APE = \rho g(z - z_*) \tag{19}$$

to isolate the irreversible mixing at the end state of $KE \rightleftharpoons PE$ in Boussinesq flows, representing the potential energy released when a disturbed density profile adiabatically returns to a monotonically decreasing (z_*) state. Tailleux (2009, 2013) later showed that the volume-averaged net dissipation of APE can be expressed in compressible flows as the time average

$$\overline{D}_{APE} = \overline{\int (\mathcal{W}_b - \mathcal{W}_{pv})dt} \tag{20}$$

over the duration of the event. The resulting mixing parameters are given by

$$\gamma_{APE} = \frac{\overline{D}_{APE}}{\overline{D}_{KE}} \quad \text{and} \quad R_{f|APE} = \frac{\overline{D}_{APE}}{\overline{D}_{APE} + \overline{D}_{KE}}, \tag{21}$$

where

$$\overline{D}_{KE} = \overline{\int \mathcal{E}\, dt}. \tag{22}$$

We can also assess irreversible mixing efficiency with the entropy production constituents via

$$\gamma_S = \frac{\int \langle \chi/T^2 \rangle dt}{\int \langle \epsilon/T \rangle dt} \quad \text{and} \quad R_{f|S} = \frac{\int \langle \chi/T^2 \rangle dt}{\Delta S}. \tag{23}$$

These mixing assessments and their input parameters are shown together in Table 1 as an event summary for both cases.

The resulting mixing efficiency parameters demonstrate both increased energetic extraction and reduced efficiency of extraction where T&K dynamics occur. The most direct efficiency assessment yields $\gamma_E \approx 0.3$ for both DNS, consistent with the typical range of $\gamma_E = 0.2$–0.3 seen in atmospheric and oceanic observations (see e.g., Gregg et al., 2018; Lozovatsky & Fernando, 2013, and citations therein). The T&K-allowing DNS generates 10% more PE than the T&K-prohibiting DNS in its final state, but it does so with 6% lower γ_E due to its 17% larger ΔKE. The flux-based $\gamma_{\mathcal{W}}$ and ΔKE partition-based γ_{KE} indicate a higher mixing efficiency of ∼0.5–0.6, with $R_{f|\mathcal{W}}$ and $R_{f|KE}$ values of ∼0.3–0.4 closer to γ_E. The 19% reduced $\gamma_{\mathcal{W}}$ and 13% reduced $R_{f|\mathcal{W}}$ in the T&K-allowing DNS stem from 31% larger extractions of $\mathcal{E}$ with only slightly (6%) larger $\int \mathcal{W}_b$. The inclusion of $\mathcal{W}_{pv}$ in γ_{KE} and $R_{f|KE}$ yields mild efficiency increases in both cases owing to small, net positive $\mathcal{W}_{pv}$ work in the expanded final state, which decreases the assessed available flux energy when compressible effects are considered. The dissipation based metrics γ_{APE} and $R_{f|APE}$ exhibit higher efficiencies of $\gamma \approx 0.9$ and $R_f \approx 0.5$ for the T&K-prohibiting DNS, while the entropy-based metrics γ_S and $R_{f|S}$ have comparable efficiency ranges ($\gamma \approx 0.5$–0.6, $R_f \approx 0.3$–0.4) to the flux and KE partition-based metrics in both cases. In all the efficiency metrics, the larger accumulated $\mathcal{E}$ in the T&K-allowing event reduces γ and R_f relative to the T&K-prohibiting case. These varied mixing efficiency assessments ultimately fail to capture the heightened energetic exchange, dissipation, and entropy production occurring in T&K events.

A more suitable mixing efficiency comparison between the two cases can be constructed by isolating the reversible components of their net energy exchange terms. Figure 10 shows the total $KE \Leftrightarrow IE$ and $KE \Leftrightarrow PE$ energy transfers for both cases decomposed into positive ($KE\Rightarrow$) and negative ($KE\Leftarrow$) components of integrated ($\mathcal{E} - \mathcal{W}_{pv}$) and $\mathcal{W}_b$. Since both transfers are net positive, the canceled-out negative energy transfer indicates how

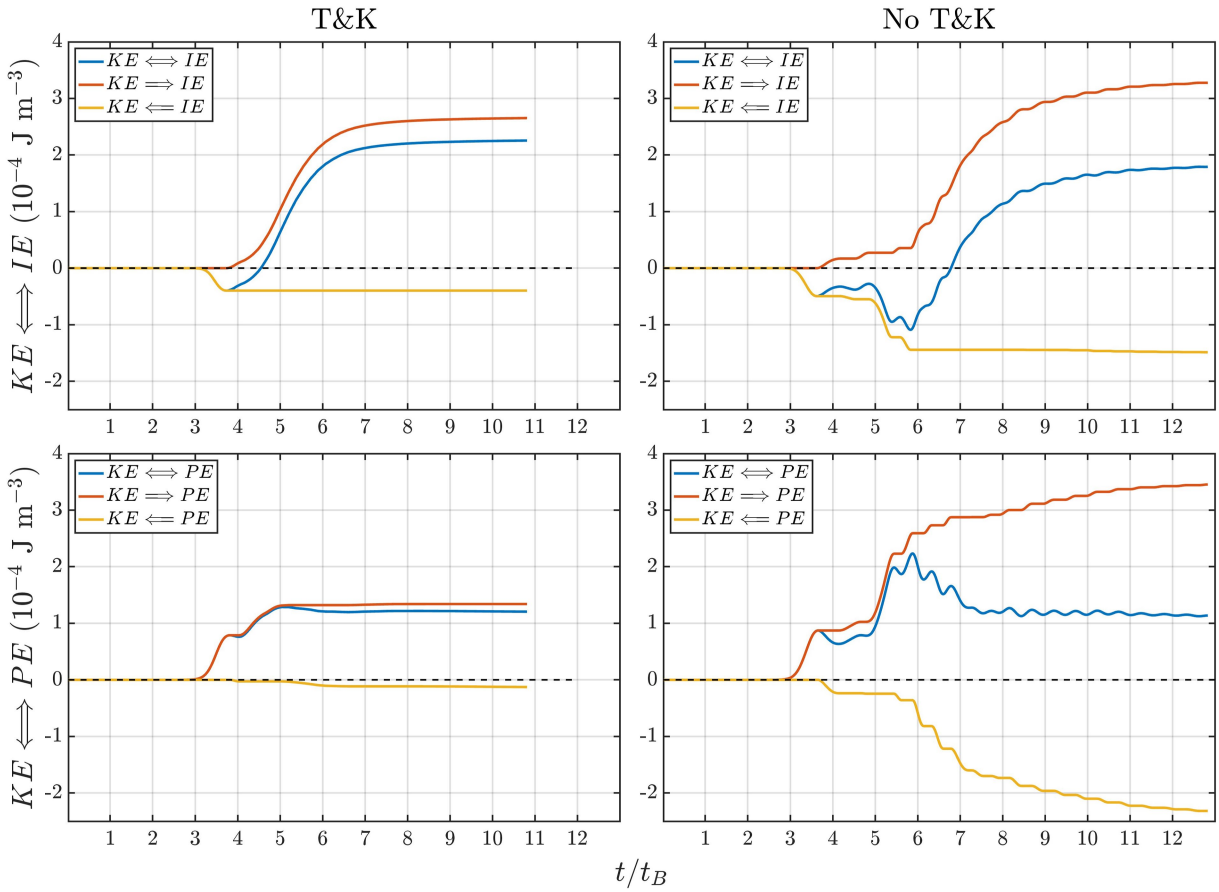

Figure 10. Comparing the total (⇔), positive (⇒), and negative (⇐) components of integrated energy transfer from *KE* with and without T&K.

much of the positive energy transfer is reversed in the final state and can be assessed as a mixing inefficiency. In $KE \rightleftharpoons PE$, $KE \leftharpoondown PE$ represents vertically displaced particles returning from their displaced altitude rather than dissipating. In $KE \rightleftharpoons IE$, $KE \leftharpoondown IE$, represents compressed regions adjacent to the expanding billows returning to their original pressure and volume as the KHI dissipate and mix with the surrounding fluid. These components reveal vastly larger reversed (i.e., wasted) energy transfers in the T&K-prohibiting DNS, where 45% of $KE \rightharpoonup IE$ is reversed (vs. 15%) and 67% of $KE \rightharpoonup PE$ is reversed (vs. 9%). As a mixing efficiency metric, the amount of retained energy transfer can be expressed as

$$\gamma_{\{IE,PE\}} = \frac{KE \rightleftharpoons \{IE,PE\}}{KE \rightharpoonup \{IE,PE\}} \quad \text{and} \quad R_{f\{IE,PE\}} = \frac{KE \rightleftharpoons \{IE,PE\}}{KE \rightharpoonup \{IE,PE\} - KE \leftharpoondown \{IE,PE\}}, \tag{24}$$

where the values for the T&K-prohibiting (allowing) DNS are $\gamma_{IE} = 0.55$ (0.85, +56%), $R_{fIE} = 0.38$ (0.74, +97%), $\gamma_{PE} = 0.33$ (0.90, +173%), and $R_{fPE} = 0.20$ (0.82, +317%).

4. Summary and Conclusions

DNS presented in this study evaluate the impact of T&K dynamics on a thermospheric KHI event observed on 26 January 2018 over Poker Flat, Alaska. The instability event was triggered by elevated shear and temperature perturbations from a local 4 km λ_z shear/stability enhancement superposed on a 16 km λ_z background IGW. Initial conditions generated from available observations reproduced the underlying 800 m layer having $Ri_{\min} = 0.05$ and Re = 2,200. Identically initialized DNS were conducted in two spanwise box sizes to assess the instability and mixing consequences when KHI are not constrained to axial uniformity as in prior studies.

DNS allowing T&K dynamics reveal unique instability pathways that evolve faster turbulence transitions and yield more vigorous dissipation and mixing than morphologies evolving from axially uniform KHI. Spanwise-billow

distortions and misaligned billow junctions seed superpositions of billow linking vortex tubes and billow merging vortex knots consistent with morphologies identified by Fritts, Wang, Lund, and Thorpe (2022) and Fritts, Wang, Thorpe, and Lund (2022). These superposed T&K features develop mode 1 and mode 2 twist wave evolutions that fragment their parent features into smaller intertwined vortex filaments with further elevated magnitudes. This rapid progression to small scales stemming from initial T&K sites yields expanding turbulence regions that quickly engulf the entire horizontal extent of the shear layer.

Cross-section comparisons with axially uniform KHI show T&K dynamics having faster fine-scale feature evolution and locally larger dissipation. Faster turbulence precludes the development of billow merging and secondary CI/KHI, dominant evolutions in the T&K-prohibiting case that were previously thought to ubiquitously drive the turbulent transition in all stratified shear turbulence scenarios. In the absence of T&K, weaker turbulence damps dissipation as fluid parcels are repeatedly stirred about the billow cores rather than mixed.

The resulting macro-scale dissipation and energy exchanges conclusively quantify the capacity for T&K instability events to contribute to elevated mixing in the thermosphere and beyond, with far-reaching implications. T&K dynamics produce 94% (44%) larger peak $\mathcal{E}$ ($\mathcal{X}$) values 1.8 t_B (1.2 t_B) faster than axially uniform KHI. Billow pairing and slowly evolving secondary CI/KHI in the T&K-prohibiting DNS yield oscillating $\mathcal{W}_b$ and weaker, stepped evolutions of $\mathcal{E}$ and $\mathcal{X}$. Over the whole event, T&K dynamics accumulate 17% more ΔKE, 31% more $\mathcal{E}$, 26% more $KE \rightleftharpoons IE$, 70% more $\overline{D}_{KE}$, and 31% more $\int \langle \epsilon \,/\, T \rangle$ than the T&K-prohibiting DNS, but they only yield 10% more ΔPE, 6% more $KE \rightleftharpoons PE$, 1% less $\overline{D}_{APE}$, and 8% more $\int \left\langle \chi \,/\, T^2 \right\rangle$. Consequently, γ and R_f values are 6–42% smaller and $10-28\%$ smaller, respectively, in the T&K-allowing DNS despite displaying more mixing in every assessed standard metric. However, it is noteworthy that the T&K-allowing DNS retains a much greater fraction of its reversible energy exchanges (56% greater γ_{IE}, 173% greater γ_{PE}), suggesting that other mixing metrics may be valuable for assessing the relative impact of different instability dynamics in the same environment.

The results of this study demonstrate that T&K dynamics dominate the turbulent transition, extracting more energy and entropy more quickly from an existing background environment than idealized, axially uniform KHI. T&K-induced twist waves, not secondary CI/KHI, are shown to be the primary drivers of turbulence and dissipation in atmospheric shear-driven flows. As such, studies of artificially constrained, axially uniform KHI in narrow spanwise lab and simulation experiments severely underestimate the mixing implications of KHI and inflate the importance of secondary CI/KHI and billow pairing in atmospheric and oceanic flows. T&K events produce stronger mixing than axially uniform KHI but do so with reduced efficiency, converting a lower fraction (but larger net amount) of the available kinetic energy into potential energy. Standard mixing efficiency metrics do not capture the enhanced irreversible mixing of T&K events, suggesting that more evaluation is needed of prevailing mixing metrics and available energy concepts to capture T&K impacts in GCM turbulence parameterizations.

Data Availability Statement

- Data: The CGCAM simulation data and Poker Flat lidar data presented in this manuscript are publicly available on Figshare (Mixa, 2023). Rocketsonde wind data were downloaded from (R. Mesquita, 2020).
- Software: Figures were made with Matlab version 2022b available under the Matlab license at https://www.mathworks.com/products/matlab.html utilizing the Climate Data Toolbox for Matlab (Greene et al., 2019).

Acknowledgments
Research described here was supported by MURI Grant FA9550-18-1-0009 and NSF Grants AGS-2230482 and AGS-2128443. Poker Flat lidar data was provided by Bifford Williams. We also acknowledge the support of the DoD High Performance Computing Modernization Program (HPCMP) for access to several supercomputer platforms that enabled the simulations reported here.

References

Barat, J. (1982). Some characteristics of clear-air turbulence in the middle stratosphere. *Journal of the Atmospheric Sciences*, *39*(11), 2553–2564. https://doi.org/10.1175/1520-0469(1982)039<2553:scocat>2.0.co;2

Caulfield, C. P., & Kerswell, R. R. (2000). The nonlinear development of three-dimensional disturbances at hyperbolic stagnation points: A model of the braid region in mixing layers. *Physics of Fluids*, *12*(5), 1032–1043. https://doi.org/10.1063/1.870358

Doddi, A., Lawrence, D., Fritts, D., Wang, L., Lund, T., Brown, W., et al. (2021). Instabilities, dynamics, and energetics accompanying atmospheric layering (ideal) campaign: High-resolution in situ observations above the nocturnal boundary layer. In *Atmospheric Measurement Techniques Discussions* (pp. 1–33).

Dong, W., Fritts, D. C., Lund, T. S., Wieland, S. A., & Zhang, S. (2020). Self-acceleration and instability of gravity wave packets: 2. Two-dimensional packet propagation, instability dynamics, and transient flow responses. *Journal of Geophysical Research: Atmospheres*, *125*(3), e2019JD030691. https://doi.org/10.1029/2019JD030691

Felten, F. N., & Lund, T. S. (2006). Kinetic energy conservation issues associated with the collocated mesh scheme for incompressible flow. *Journal of Computational Physics*, *215*(2), 465–484. https://doi.org/10.1016/j.jcp.2005.11.009

Fritts, D. C., Baumgarten, G., Wan, K., Werne, J. A., & Lund, T. S. (2014). Quantifying Kelvin-Helmholtz instability dynamics observed in noctilucent clouds: 2. Modeling and interpretation of observations. *Journal of Geophysical Research: Atmospheres*, *119*(15), 9359–9375. https://doi.org/10.1002/2014JD021833

Fritts, D. C., & Dunkerton, T. J. (1985). Fluxes of heat and constituents due to convectively unstable gravity waves. *Journal of the Atmospheric Sciences*, *42*(6), 549–556. https://doi.org/10.1175/1520-0469(1985)042<0549:fohacd>2.0.co;2

Fritts, D. C., Lund, A. C., Lund, T. S., & Yudin, V. (2022). Impacts of limited model resolution on the representation of mountain wave and secondary gravity wave dynamics in local and global models. 1: Mountain waves in the stratosphere and mesosphere. *Journal of Geophysical Research: Atmospheres*, *127*(9), e2021JD035990. https://doi.org/10.1029/2021jd035990

Fritts, D. C., & Wang, L. (2013). Gravity wave–fine structure interactions. Part II: Energy dissipation evolutions, statistics, and implications. *Journal of the Atmospheric Sciences*, *70*(12), 3735–3755. https://doi.org/10.1175/JAS-D-13-059.1

Fritts, D. C., Wang, L., Baumgarten, G., Miller, A. D., Geller, M. A., Jones, G., et al. (2017). High-resolution observations and modeling of turbulence sources, structures, and intensities in the upper mesosphere. *Journal of Atmospheric and Solar-Terrestrial Physics*, *1–22*, 57–78. https://doi.org/10.1016/j.jastp.2016.11.006

Fritts, D. C., Wang, L., Lund, T., & Thorpe, S. (2022). Multi-scale dynamics of Kelvin–Helmholtz instabilities. Part 1. Secondary instabilities and the dynamics of tubes and knots. *Journal of Fluid Mechanics*, *941*, A30. https://doi.org/10.1017/jfm.2021.1085

Fritts, D. C., Wang, L., Thorpe, S., & Lund, T. (2022). Multi-scale dynamics of Kelvin–Helmholtz instabilities. Part 2. Energy dissipation rates, evolutions and statistics. *Journal of Fluid Mechanics*, *941*, A31. https://doi.org/10.1017/jfm.2021.1086

Fritts, D. C., Wang, L., & Werne, J. A. (2013). Gravity wave–fine structure interactions. Part I: Influences of fine structure form and orientation on flow evolution and instability. *Journal of the Atmospheric Sciences*, *70*(12), 3710–3734. https://doi.org/10.1175/jas-d-13-055.1

Fritts, D. C., Wieland, S. A., Lund, T. S., Thorpe, S. A., & Hecht, J. H. (2021a). Kelvin-Helmholtz billow interactions and instabilities in the mesosphere over the Andes Lidar observatory: 2. Modeling and interpretation. *Journal of Geophysical Research: Atmospheres*, *126*(1), e2020JD033414. https://doi.org/10.1029/2020JD033412

Garcia, R. R., López-Puertas, M., Funke, B., Marsh, D. R., Kinnison, D. E., Smith, A. K., & González-Galindo, F. (2014). On the distribution of CO_2 and co in the mesosphere and lower thermosphere. *Journal of Geophysical Research*, *119*(9), 5700–5718. https://doi.org/10.1002/2013JD021208

Garcia, R. R., Marsh, D. R., Kinnison, D. E., Boville, B. A., & Sassi, F. (2007). Simulation of secular trends in the middle atmosphere, 1950-2003. *Journal of Geophysical Research*, *112*(D9), D09301. https://doi.org/10.1029/2006JD007485

Gardner, C. S. (2018). Role of wave-induced diffusion and energy flux in the vertical transport of atmospheric constituents in the mesopause region. *Journal of Geophysical Research: Atmospheres*, *123*(12), 6581–6604. https://doi.org/10.1029/2018JD028359

Greene, C. A., Thirumalai, K., Kearney, K. A., Delgado, J. M., Schwanghart, W., Wolfenbarger, N. S., et al. (2019). The climate data toolbox for MATLAB. *Geochemistry, Geophysics, Geosystems*, *20*(7), 3774–3781. https://doi.org/10.1029/2019gc008392

Gregg, M. C., D'Asaro, E. A., Riley, J. J., & Kunze, E. (2018). Mixing efficiency in the ocean. *Annual Review of Marine Science*, *10*(1), 443–473. https://doi.org/10.1146/annurev-marine-121916-063643

Hecht, J. H., Fritts, D. C., Gelinas, L. J., Rudy, R. J., Walterscheid, R. L., & Liu, A. Z. (2021). Kelvin-Helmholtz billow interactions and instabilities in the mesosphere over the Andes Lidar observatory: 1. Observations. *Journal of Geophysical Research: Atmospheres*, *126*. e2020JD033414. https://doi.org/10.1029/2020JD033414

Jeong, J., & Hussain, F. (1995). On the identification of a vortex. *Journal of Fluid Mechanics*, *285*, 69–94. https://doi.org/10.1017/s0022112095000462

Kantha, L., Lawrence, D., Luce, H., Hashiguchi, H., Tsuda, T., Wilson, R., et al. (2017). Shigaraki UAV-radar experiment (ShUREX): Overview of the campaign with some preliminary results. *Progress in Earth and Planetary Science*, *4*(1), 1–26. https://doi.org/10.1186/s40645-017-0133-x

Kelvin, W. (1880). Vibrations of a columnar vortex. *Philosophical Magazine*, *10*, 155–168.

Klaassen, G., & Peltier, W. (1985). The onset of turbulence in finite-amplitude Kelvin–Helmholtz billows. *Journal of Fluid Mechanics*, *155*, 1–35. https://doi.org/10.1017/s0022112085001690

Lehmacher, G., Scott, T., Larsen, M., Bilén, S., Croskey, C., Mitchell, J., et al. (2011). The turbopause experiment: Atmospheric stability and turbulent structure spanning the turbopause altitude. *Annales Geophysicae*, *29*(12), 2327–2339. https://doi.org/10.5194/angeo-29-2327-2011

Liu, H. L. (2000). Temperature changes due to gravity wave saturation. *Journal of Geophysical Research*, *105*(D10), 12329–12336. https://doi.org/10.1029/2000JD900054

Liu, H. L. (2021). Effective vertical diffusion by atmospheric gravity waves. *Geophysical Research Letters*, *48*, 1–10. https://doi.org/10.1029/2020GL091474

Lozovatsky, I., & Fernando, H. (2013). Mixing efficiency in natural flows. *Philosophical Transactions of the Royal Society A: Mathematical, Physical & Engineering Sciences*, *371*(1982), 20120213. https://doi.org/10.1098/rsta.2012.0213

Lund, T. S., Fritts, D. C., Wan, K., Laughman, B., & Liu, H. L. (2020). Numerical simulation of mountain waves over the southern Andes. Part I: Mountain wave and secondary wave character, evolutions, and breaking. *Journal of the Atmospheric Sciences*, *77*(12), 4337–4356. https://doi.org/10.1175/JAS-D-19-0356.1

McIntyre, M. E. (1989). On dynamics and transport near the polar mesopause in summer. *Journal of Geophysical Research*, *94*(D12), 14617–14628. https://doi.org/10.1029/jd094id12p14617

Mesquita, R. (2020). Mesquita et al 2020 (1.2) [Dataset]. Zenodo. https://doi.org/10.5281/zenodo.3905282

Mesquita, R. L., Larsen, M. F., Azeem, I., Stevens, M. H., Williams, B. P., Collins, R. L., & Li, J. (2020). In situ observations of neutral shear instability in the statically stable high-latitude mesosphere and lower thermosphere during quiet geomagnetic conditions. *Journal of Geophysical Research: Space Physics*, *125*(8), 1–14. https://doi.org/10.1029/2020JA027972

Mixa, T. (2023). Mixa et al., 2023 data repository. Figshare [Dataset]. https://doi.org/10.6084/m9.figshare.22814600

Moin, P., & Mahesh, K. (1998). Direct numerical simulation: A tool in turbulence research. *Annual Review of Fluid Mechanics*, *30*(1), 539–578. https://doi.org/10.1146/annurev.fluid.30.1.539

Osborn, T. (1980). Estimates of the local rate of vertical diffusion from dissipation measurements. *Journal of Physical Oceanography*, *10*(1), 83–89. https://doi.org/10.1175/1520-0485(1980)010<0083:eotlro>2.0.co;2

Osborn, T. R., & Cox, C. S. (1972). Oceanic fine structure. *Geophysical Fluid Dynamics*, *3*(4), 321–345. https://doi.org/10.1080/03091927208236085

Peltier, W., & Caulfield, C. (2003). Mixing efficiency in stratified shear flows. *Annual Review of Fluid Mechanics*, *35*(1), 135–167.

Pope, S. B. (2000). *Turbulent flows* (Vol. 1). Cambridge University Press. https://doi.org/10.1017/CBO9780511840531

Sato, T., & Woodman, R. F. (1982). Fine altitude resolution observations of stratospheric turbulent layers by the Arecibo 430 MHz radar. *Journal of the Atmospheric Sciences*, *39*(11), 2546–2552. https://doi.org/10.1175/1520-0469(1982)039<2546:faroos>2.0.co;2

Swenson, G., Yee, Y., Vargas, F., & Liu, A. (2018). Vertical diffusion transport of atomic oxygen in the mesopause region consistent with chemical losses and continuity: Global mean and inter-annual variability. *Journal of Atmospheric and Solar-Terrestrial Physics*, *178*, 47–57. https://doi.org/10.1016/j.jastp.2018.05.014

Tailleux, R. (2009). On the energetics of stratified turbulent mixing, irreversible thermodynamics, Boussinesq models and the ocean heat engine controversy. *Journal of Fluid Mechanics*, *638*, 339–382. https://doi.org/10.1017/S002211200999111X

Tailleux, R. (2013). Irreversible compressible work and available potential energy dissipation in turbulent stratified fluids. *Physica Scripta*, *88*(T155), 014033. https://doi.org/10.1088/0031-8949/2013/T155/014033

Thorpe, S. A. (1987). Transitional phenomena and the development of turbulence in stratified fluids: A review. *Journal of Geophysical Research*, *92*(C5), 5231–5248. https://doi.org/10.1029/jc092ic05p05231

Thorpe, S. A. (2002). The axial coherence of Kelvin–Helmholtz billows. *Quarterly Journal of the Royal Meteorological Society*, *128*(583), 1529–1542. https://doi.org/10.1002/qj.200212858307

Weinstock, J. (1978). Vertical turbulent diffusion in a stably stratified fluid. *Journal of the Atmospheric Sciences*, *35*(6), 1022–1027. https://doi.org/10.1175/1520-0469(1978)035<1022:vtdias>2.0.co;2

White, F. M. (1974). *Viscous fluid flow*. McGraw-Hill.

Winters, K. B., Lombard, P. N., Riley, J. J., & D'Asaro, E. A. (1995). Available potential energy and mixing in density-stratified fluids. *Journal of Fluid Mechanics*, *289*, 115–128. https://doi.org/10.1017/s002211209500125x